High-Purity Fe₃S₄ Greigite Microcrystals for Magnetic and Electrochemical Performance

Guowei Li,[†] Baomin Zhang,[‡] Feng Yu,[§] Alla A. Novakova,[∇] Maxim S. Krivenkov,[∇] Tatiana Y. Kiseleva,[∇] Liao Chang,[○] Jiancun Rao,[⊥] Alexey O. Polyakov,[†] Graeme R. Blake,[†] Robert A. de Groot,[‡] and Thomas T. M. Palstra*,[†]

[†]Zernike Institute for Advanced Materials, University of Groningen, Nijenborgh 4, 9747 AG Groningen, The Netherlands

[‡]Institute for Molecules and Materials, Radboud University Nijmegen, Heyendaalseweg 135, 6525 AJ Nijmegen, The Netherlands

[§]Institute of Chemical and Engineering Sciences, Agency for Science, Technology and Research (A*STAR), Pesek Road, 627833, Jurong Island, Singapore

[∇]Faculty of Physics, Lomonosov Moscow State University, Leninskie Gory, Moscow, 119899, Russian Federation

[○]Department of Earth Sciences, Utrecht University, Budapestlaan 17, 3584 CD Utrecht, The Netherlands

[⊥]School of Materials Science and Engineering, Harbin Institute of Technology, 150001 Harbin, People's Republic of China

S *Supporting Information*

ABSTRACT: High-purity Fe₃S₄ (greigite) microcrystals with octahedral shape were synthesized via a simple hydrothermal method using a surfactant. The as-prepared samples have the inverse spinel structure with high crystallinity. The saturation magnetization (M_s) reaches 3.74 μ_B at 5 K and 3.51 μ_B at room temperature, which is larger than all reported values thus far. Electrical transport measurements show metallic behavior with a resistivity 40 times lower than in any previous report. The potential use of greigite as an anode in lithium-ion batteries was investigated by cyclic voltammery and galvanostatic discharge−charge cycling on as-prepared samples. The discharge capacity was 1161 mAh/g in the first cycle and 563 mAh/g in the 100th cycle. This excellent electrochemical performance can be attributed to the high purity, crystallinity, and favorable morphology of the products.
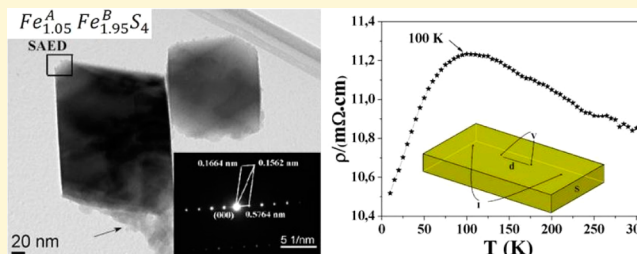
1. INTRODUCTION

Greigite (Fe₃S₄) was discovered in silt and clay sediments in California in 1964.[1] Its formation accompanies the decomposition of organic matter in the biogeochemical and bacterial sulfate reduction process.[2] However, greigite was initially believed to be palaeomagnetically unimportant, because of its thermodynamic metastability and the lack of any lasting record on geological time scales.[3] This traditional viewpoint changed when greigite was discovered in the sediments of Loch Lomond, indicating greater thermodynamic stability than previously proposed.[4,5] Interestingly, greigite provides clues in the search for life on Mars. In the Martian meteorite ALH84001, which is proposed to have crystallized from molten rock 4 billion years ago, an elongated multicrystalline core of greigite was found inside an organic envelope.[6,7] This may be from the fossil remains of Martian biota.

Greigite is also of interest in modern material science. Recent band structure calculations revealed that Fe₃S₄ shows a complex Fermi surface with a unique influence of relativistic effects: two sheets of the Fermi surface (dis)appear, depending on the direction of an applied magnetization. This enables spintronics on the level of a single compound, rather than using traditional heterostructure devices.[8] Fe₃S₄ is also a potential anode material in lithium-ion batteries (LIBs). The use of Fe₃O₄ in LIBs has been researched extensively, because of its high theoretical capacity.[9] As discussed later, Fe₃S₄ has a theoretical capacity of 785 mAh/g, two times higher than the conventional anode material graphite (372 mAh/g). Considering that greigite is nontoxic and abundant, it is an ideal material for high-performance LIBs. Furthermore, greigite also has potential applications in hydrogen storage, cancer hyperthermia, and magnetic guided delivery of drugs.[10−12]

Greigite is an iron thiospinel and has the same inverse spinel structure as its oxide counterpart magnetite, Fe₃O₄. The crystallographic structure of Fe₃S₄ is displayed in Figure 1. The unit cell consists of eight Fe₃S₄ moieties (space group: $Fd\bar{3}m$). The S atoms form a face-centered-cubic lattice, in which 1/8 of the tetrahedral A-sites are occupied by Fe³⁺ and 1/2 of the octahedral B-sites are equally occupied by Fe²⁺ and Fe³⁺. A neutron powder diffraction study indicated a collinear
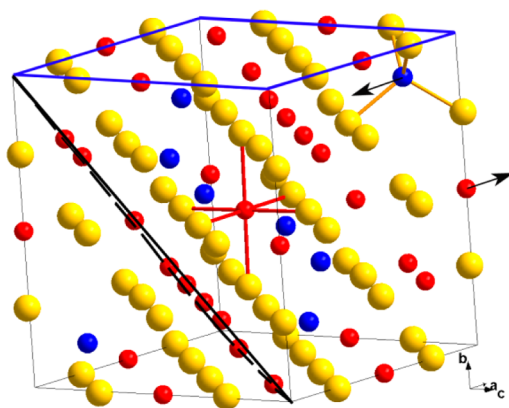
Figure 1. Crystal structure of Fe_3S_4 with the (001) and (111) planes outlined in blue and black, respectively. Sulfur atoms (yellow spheres) form a cubic close-packed lattice: 1/8 of the tetrahedral A sites are occupied by Fe^{3+} (blue spheres) and 1/2 of the octahedral B sites are occupied by Fe^{2+} and Fe^{3+} (red spheres) equally. The magnetic moments on the A and B sites are antiparallel and aligned along the [100] crystallographic axis (indicated by arrows).

ferromagnetic structure in which the iron moments on the tetrahedral and octahedral sites are antiparallel.[13] No spin canting or significant cation vacancy concentration was observed for either sublattice.[14] It is generally accepted that the magnetic easy axis of greigite is [100] at all temperatures, rather than the [111] direction of magnetite. However, there is no exact experimental confirmation.[15]

Despite the above-mentioned studies, greigite has received much less attention than well-studied Fe_3O_4, because of its metastable nature. It has been demonstrated that Fe_3S_4 is converted to a mixture of pyrrhotite ($Fe_{1−x}S$) and either pyrite (FeS_2) or sulfur when heated in air at temperatures in the range of 180−200 °C, and finally to Fe_3O_4 and maghemite (γ-Fe_2O_3). Although it is relatively stable in argon gas, Fe_3S_4 still decomposes above 250 °C.[16] The absence of pure samples of either natural or synthetic greigite has thus far hindered precise determinations of its physical and chemical properties, including saturation magnetization (M_s), Curie temperature (T_c), the first anisotropy constant (K_1), and the electrical conductivity. Several synthesis methods have recently been reported. Akhtar et al.[17] prepared precursor dithiocarbamato Fe^{3+} complexes and then performed thermolysis in oleylamine at different temperatures. Greigite was always the dominant product but often coexisted with a lower concentration of FeS. Zhang et al.[18] prepared relatively pure Fe_3S_4 nanoparticles by heating a $Fe(Ddtc)_3$ (Ddtc = diethyldithiocarbamate) precursor in an oleic acid/oleylamine/1-octadecene solvent. Hydrothermal methods, which are carried out at high pressure (>2 MPa) and low temperature (<300 °C) have been widely used in the synthesis of nanoarchitectured materials.[19,20] For example, a hydrothermal method in an external magnetic field allowed either greigite or marcasite (FeS_2) to be selectively synthesized in the form of microrods.[21] Using a similar method, Chang et al.[22] synthesized polycrystalline greigite. It is difficult to obtain pure synthetic greigite because most procedures simultaneously produce other iron sulfides such as mackinawite (FeS) and pyrite (FeS_2). This is often apparent in previous reports from poor-quality X-ray diffraction (XRD) patterns that contain impurity peaks and broad greigite peaks that imply poor crystallinity. Low M_s values of the saturation magnetization also imply poor quality samples, with, in most cases,

$M_s < 2.5$ μ_B per formula unit (f.u.), compared to the expected value of 4 μ_B/f.u.[23−25] (see summary in ref 24).

Herein, a simple hydrothermal method is developed to synthesize high purity greigite. By carefully controlling the reaction temperature, reaction time, and the quantity of surfactant, greigite microcrystals with a (truncated) octahedral shape and size ∼1 μm can be synthesized. The as-prepared product has a larger saturation magnetization and lower resistivity than all previous reports. The performance of high-purity greigite as an anode material in LIBs is also studied. A high capacity is maintained up to 100 cycles, making it an excellent prospective electrode material.

2. METHOD

2.1. Synthesis. Nitrogen gas was bubbled for at least 30 min through 35 mL of H_2O to remove all dissolved oxygen before the synthesis. In a typical experiment, (0.6 mmol, 0.2187 g) of the surfactant cetrimonium bromide (CTAB) was dissolved in the water under continuous stirring to form a solution. After 10 min, (3 mmol, 0.365 g) of L-cysteine and (2 mmol, 0.2535 g) of $FeCl_2$ were added to the solution. The solution was stirred for another 10 min, and then transferred into a 50 mL Teflon-sealed autoclave. The autoclave was kept at 165 °C for 40 h before being cooled to room temperature in air. A black precipitate was collected and washed with distilled water and ethanol three times. Finally, the product was heated at 60 °C under vacuum for 8 h.

2.2. Characterization. Room-temperature powder X-ray diffraction (XRD) data were recorded with a Bruker D8 Advance diffractometer equipped with a Cu Kα source (λ = 0.15406 nm). XRD data at 20 K were collected using a Huber G670 diffractometer operating with Cu Kα radiation and equipped with a closed-cycle refrigerator. The morphology and crystal structure were examined using a Philips XL 30 scanning electron microscope (SEM) and a JEM 2010F transmission electron microscope (TEM) operated at an accelerating voltage of 200 kV. The magnetization was measured using a Quantum Design MPMS-XL7 SQUID magnetometer. Mössbauer spectra were measured at room and liquid nitrogen temperatures using a constant acceleration spectrometer MS-1104 M with a ^{57}Co(Rh) radiation source. For measurement of the electronic properties, a rectangular-shaped polycrystalline sample was prepared by pressing Fe_3S_4 particles under 3 × 10^7 Pa pressure for 15 min. The electrical contacts were made using Pt wire (0.05 mm in diameter) connected to the sample by silver paint. The measurements were performed using a commercial Quantum Design Physical Properties Measurement System (PPMS) and an Agilent 3458a multimeter. Raman spectra were measured in a backscattering configuration using a liquid-nitrogen-cooled charged coupled device (CCD) connected to a three-grating micro-Raman spectrometer (Model T6400, Jobin Yvon). The incident laser power was limited to 0.5 mW to avoid oxidation of the sample using excitation wavelengths of 632.8 nm.

Details of phonon calculations related to the Raman spectroscopy are described in the Supporting Information.

2.3. Electrochemical Measurements. To fabricate the anode of a coin cell battery, the as-obtained Fe_3S_4 powder was mixed with acetylene black and polyvinylidene fluoride (PVDF) in a weight ratio of 80:10:10 in N-methyl-2 pyrrolidinone (NMP). The obtained slurry was coated onto copper foil, dried at 120 °C for 12 h, and then punched into round plates 12.0 mm in diameter to form anode electrodes. Finally, the prepared anode, a Celgard2400 separator (diameter of 16.0 mm), a lithium cathode, and an electrolyte consisting of 1 M $LiPF_6$ in ethylene carbonate (EC)/diethyl carbonate (DEC)/ethyl methyl carbonate (EMC) (1:1:1 vol %) were assembled into a coin cell (CR2032) in an argon-filled glovebox (H_2O and O_2 < 1 ppm). The coin cells prepared were kept at room temperature for 10 min at 4.2 V during charging and examined using a Maccor Series 4200 standard battery test system at various charge/discharge rates between 0.01 and 3 V. Cyclic voltammetry (CV) was collected using an Autolab PGSTAT30 electrochemical workstation.

3. RESULTS AND DISCUSSION

3.1. Phase and Morphology Characterization. Observed, calculated, and difference powder XRD profiles of the obtained product at room temperature are presented in Figure 2. All the peaks can be indexed in the cubic Fe_3S_4 spinel
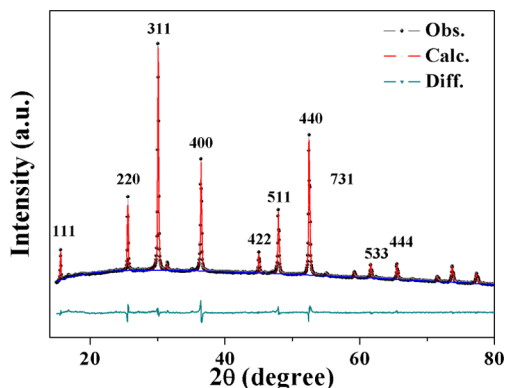
Figure 2. Observed (black data points), calculated (red line), and difference (light blue line) XRD patterns of the as-prepared sample at room temperature.

structure with space group $Fd\bar{3}m$ (PDF File Card No. 16-0713). No peaks belonging to sulfur or to other iron sulfides or oxides were observed, implying that no crystalline impurities were present at a level of >1 wt %. The refined lattice parameter was $a = 9.8719$ (1) Å, which is in good agreement with the reported value for greigite.[26] The refined atomic coordinate of sulfur on the 32e site was $x = y = z = 0.2546(1)$, in perfect agreement with calculations.[8] Other than a contraction of the unit cell, the refined structure at 20 K was essentially the same as at room temperature; details are given in the Supporting Information (Figure S1). The molar ratio of Fe to S was 2.99:4, according to energy-dispersive X-ray spectroscopy (EDS) analysis (see Figure S2 in the Supporting Information), consistent with a stoichiometric Fe_3S_4 sample. It should be noted here that the synthesis of pure, stoichiometric greigite requires carefully optimized experimental parameters. A small difference in the reaction temperature, the quantity of CTAB, and the purity of the starting materials (in particular, $FeCl_2$) will lead to the formation of second phases such as S or Fe_2O_3.

The morphology of the sample was characterized by SEM and TEM, as shown in Figure 3. The SEM images in Figure 3A reveal that the product consists of well-dispersed microcrystals with uniform (truncated) octahedral shapes. These (truncated) octahedra are fully developed and composed of eight {111} planes with a mean edge length of ~1 μm. Elemental mapping of the crystals indicates that the S and Fe are distributed homogeneously. It has been demonstrated that greigite is very sensitive to oxygen and can be oxidized to iron oxide, especially under wet conditions.[16] However, we did not detect oxygen on the surface of the crystals, which implies that high-purity greigite is more stable than expected. In accordance with the SEM results, TEM images (Figure 3B) show the morphology of the crystals in more detail. The selected area electron diffraction (SAED) pattern recorded along the $[1\bar{3}4]$ zone axis direction can be uniquely indexed. Although some stacking faults can be identified in the high-resolution TEM (HRTEM) image in Figure 3C (indicated by arrows), the clear lattice fringes confirm that the entire octahedron is a single crystal. The
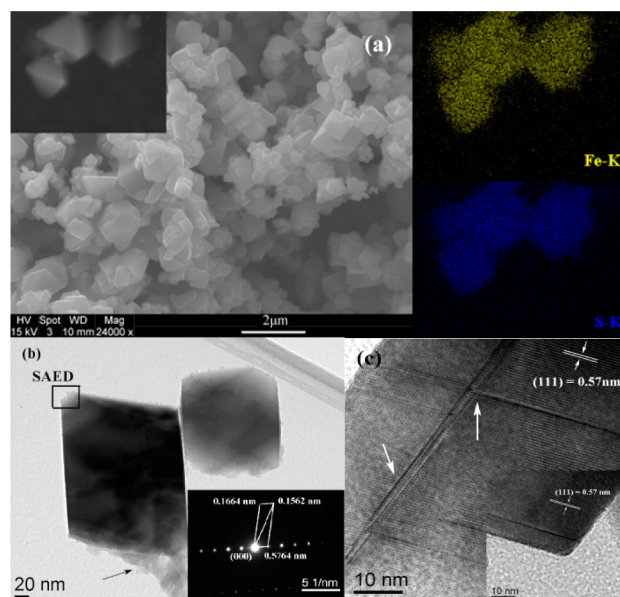

Figure 3. (A) SEM image of Fe_3S_4 crystals synthesized in this work: three typical octahedra are presented in the upper left inset, and the corresponding elemental maps are shown in the right-hand panel (yellow for Fe, and blue for S). (B) TEM image of two Fe_3S_4 crystals and corresponding SAED pattern (inset). (C) HRTEM lattice image of the edge and corner (inset) of a typical crystal.

spacing of the fringes is 0.57 nm, which corresponds well to the (111) interplanar distance in greigite.

3.2. Mössbauer Spectra. Figure 4A shows the room-temperature (RT) ^{57}Fe Mössbauer spectrum of our sample. The corresponding spectrum at 80 K is shown in Figure S3 in the Supporting Information. Both spectra were best fitted with three sextets, corresponding to one tetrahedral (A-site) and two magnetically nonequivalent octahedral (B-sites). The hyperfine interaction parameters extracted from the fits are listed in Table S1 in the Supporting Information. We did not detect signals belonging to any paramagnetic phase (FeS_2) or oxidation product (Fe_3O_4 or Fe_2O_3), in contrast to previous studies.[27] The isomer shifts for the A-site are 0.27 and 0.37 mm/s at RT and 80 K (see Figure S3 in the Supporting Information), respectively, which are attributed to the high-spin Fe^{3+} state.[28] The hyperfine field of the A-site is 3.14 T at RT, and increases slightly to 3.19 T at 80 K. The fit unambiguously indicates that only Fe^{3+} occupies the tetrahedral site in this temperature range. This implies that greigite has a fully inverse spinel structure. As shown in Table S1 in the Supporting Information, the isomer shifts of the B_a and B_b sextets are 0.53 and 0.54 mm/s at RT, and 0.67 and 0.65 mm/s at 80 K. (B_a and B_b represent the two nonequivalent B-sites, the detailed meaning of which is explained below.) Thus, both sites have the same isomer shift, within experimental error. However, the hyperfine field of the B_a site is always larger than that of the B_b site (3.14 T versus 3.05 T at RT, and 3.29 T versus 3.19 T at 80 K). The same result was recently obtained in a study of greigite nanoparticles of different sizes, but here the third sextet was attributed to the hexagonal smythite phase.[29] Smythite was first assigned the same chemical formula as greigite (Fe_3S_4),[30] but this was subsequently revised to Fe_9S_{11}.[31] The difference in symmetry between smythite and greigite means that they can easily be distinguished by XRD. Considering the high purity of our
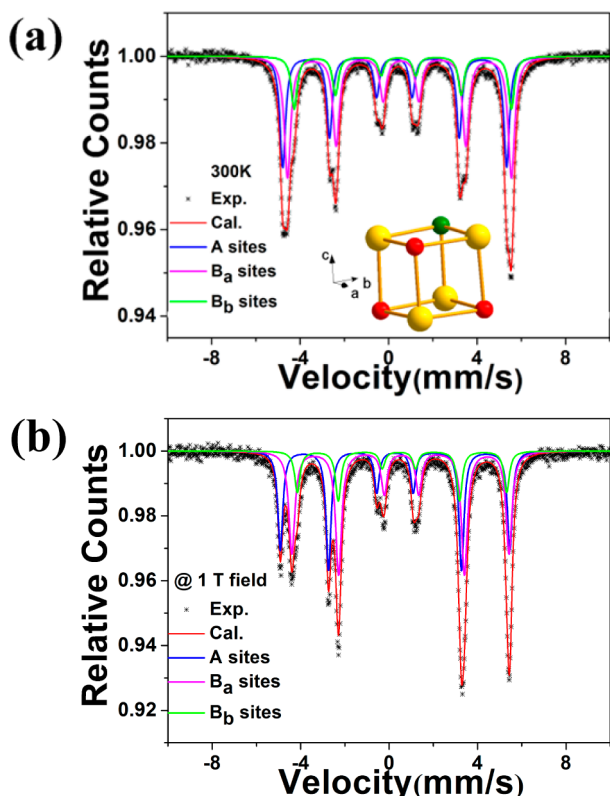
Figure 4. (A) Room-temperature (RT) ^{57}Fe Mössbauer spectrum of the Fe$_3$S$_4$ microcrystals in zero field. One octant of the cubic unit cell of greigite is shown (inset), where the yellow spheres are sulfur and the red and green spheres denote two nonequivalent octahedral site iron cations. (B) ^{57}Fe Mössbauer spectrum in a magnetic field of 1 T.

For a dominating magnetic hyperfine interaction, the Mössbauer resonance lines are shifted according to first-order perturbation theory by an amount proportional to $(3 \cos^2 \theta - 1)$, where θ is the angle between the local hyperfine field H_{hyp} and the local symmetry axis (the [111] axes for the B-site).[32] If we assume that the direction of the easy magnetization for greigite is [001] as generally accepted, then the angle between the main axis of the EFG (electric field gradient tensor) and H_{hyp} would be the same for all four Fe ions. This implies that only one sextet would be observed for the B-site, which contradicts our experimental data. If, instead, the easy magnetization direction is along the [111] direction, as in magnetite, then $\theta = 90°$ for 3/4 of the B-site cations (red spheres in Figure 4A) and $\theta = 0$ for the remaining 1/4 of the B-site cations (green sphere in Figure 4A). This will yield two B-site subspectra, with relative intensities of 3:1. For our data, the ratio is 2.6:1 at 300 K but only 1.8:1 at 80 K. Two B-site sextets with an intensity ratio of 3:1 have also been observed in Mössbauer spectra of Fe$_3$O$_4$ above the Verwey transition.[32−34] Furthermore, ferromagnetic resonance (FMR) spectroscopy on greigite indicates a negative magnetocrystalline anisotropy constant (K_1), which is the same as in magnetite.[35] In a cubic crystal, the lowest-order terms in the magnetocrystalline anisotropy energy can be written as

$$\frac{E}{V} = K_1(\alpha^2\beta^2 + \beta^2\gamma^2 + \alpha^2\gamma^2) + K_2\alpha^2\beta^2\gamma^2$$

where α, β, and γ are the direction cosines of the magnetization. Thus, the easy axis is determined by both K_1 and K_2 if K_2 is not assumed to be zero. The work of Winklhofer et al. indicates a similar value of K_2/K_1 of +0.30 to 0.33 for different anisotropy models.[36] This clearly indicates an easy axis in the [111] direction. Thus, we can conclude that greigite has an easy magnetization axis along the [111] direction, rather than the [100] direction reported in previous work. We conclude that the direction of H_{hyp}, with respect to the easy axis, is the most likely explanation for the two B-site sextets in greigite. The significant difference from the theoretical intensity ratio of 3:1 at 80 K might indicate that the easy axis moves away from [111] at low temperature; for example, a 1:1 ratio would be expected for an easy axis of [110].[32] The application of an external magnetic field aligns the spins in one direction. Indeed, this ratio increased to 2.8:1 when a magnetic field of 1 T parallel to the γ beam was applied at 300 K (Figure 4B and Table S1 in the Supporting Information).

We note that H_{hyp} for the A-site increased by 8 kOe with applied field, whereas H_{hyp} for the B$_a$- and B$_b$-sites decreased by 9 kOe and 11 kOe, respectively. This also proves that the Fe

sample, it is reasonable to assume that the third sextet is intrinsic to greigite.

The value of the isomer shift shows that valence state of the B-site iron ions is between 2+ and 3+, as it is for magnetite due to fast electron hopping. We also note that H_{hyp} for the A-site increased with applied external magnetic field, whereas H_{hyp} for the B$_a$- and B$_b$-sites decreased by nearly the same values (see Figure 4B and Table S1 in the Supporting Information).
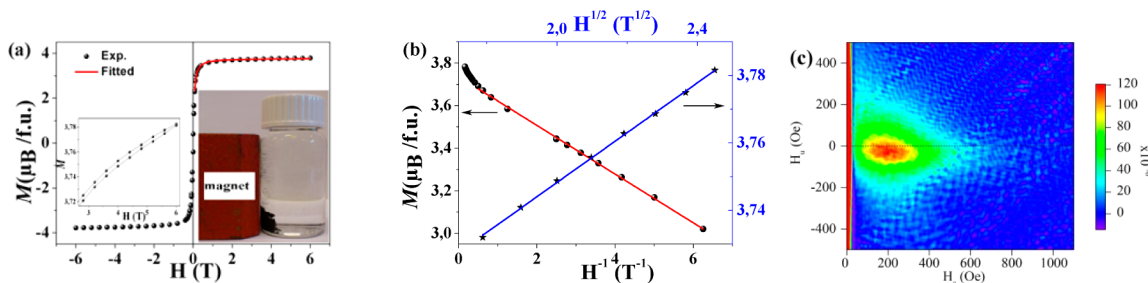
Both observations—the same isomer shifts and the same reaction to the external magnetic field—confirm that the third component of the spectra corresponds to the B-site iron ions. The nature of two nonequivalent B-site positions for magnetite is discussed in ref 29 and we tend toward the same explanation for greigite.

Figure 5. (A) Magnetization versus field loop measured at 5 K. The inset shows the magnetic separation of Fe$_3$S$_4$ crystals from aqueous solution using an external magnet. (B) Magnetization versus H^{-1} (black) and $H^{1/2}$ (blue) for the loops at 5 K. (C) First-order reversal curve (FORC) diagram of the crystals.

ions on the A- and B-sublattices are antiferromagnetically coupled via superexchange.

3.3. Magnetic Properties. Magnetic hysteresis loops at 5 K and 300 K of our greigite sample are presented in Figure 5A and Figure S4 in the Supporting Information, respectively. Typical ferrimagnetic behavior is observed in the measured temperature range, with a coercive field H_c = 92 Oe and a remanent magnetization M_r = 0.4 μ_B/f.u. at 5 K. Considering that Fe_3S_4 is a soft magnetic material, according to the hysteresis loops, and that the crystal dimension is in the micrometer scale, we can approximate the saturation magnetization with

$$M = M_s(1 - aH^{-1} - bH^{-2}) + cH^{1/2}$$

where M is the magnetization, M_s is the saturation magnetization, and a, b, and c are constants that describe the structural inhomogeneity within the sample, the magnetic anisotropy energy, and the paraeffect caused by the external field, respectively.[37] The fitting of the magnetization curves in the first quadrant for the applied field $H > H_c$ is displayed in Figure 5A, which shows excellent agreement with the experimental data. The magnetization curve is determined by microstructural inhomogeneities in the low external field range. By plotting the M versus H^{-1}, a linear relationship is obtained below 1.2 T, as shown in Figure 4B. The slope of 0.1146 Oe indicates that these microstructural inhomogeneities act as stress centers in the spin alignment around them. The deviation of the linear relationship at high field can be attributed to the paraprocess. This can be seen in the variation of M_s as a function of $H^{1/2}$ (Figure 5B) for fields of >3.2 T. Unfortunately, we cannot compare the level of inhomogeneity and the paraprocess in Fe_3S_4 with previous data in the literature. Nevertheless, we can establish precise M_s values of 3.74 μ_B (70.56 emu/g) at 5 K and 3.51 μ_B (67.16 emu/g) at RT. These values are significantly larger than in previous reports of greigite (the highest reported value was M_s = 3.4 μ_B at 5 K[13]). The high M_s allows easy separation of the greigite crystals from the solution when a magnet is placed near the glass bottle (see inset to Figure 5A). Coey et al. predicted assuming a purely ionic model that M_s should be 4 μ_B.[33] The magnetization measured in our current work approaches this value and is an indicator of the high quality of the sample. However, it is important to address the difference between our experimental and expected values. It is probable that the moment is lowered from 4 μ_B due to covalency: our recent band structure calculations predicted a magnetization of 3.38 μ_B in greigite.[8] Similar results have also been reported by other groups.[23,24] First-principle calculations based on the GGA+U model with U_{eff} = 1.16 eV give sublattice magnetizations of m_A = 3.05 μ_B and m_B = 3.25 μ_B, both of which are significantly decreased, compared with the purely ionic model. Generally, the increase in covalency is caused by the overlap of wave functions between Fe and S ions, which, from the band point of view, corresponds to a higher degree of hybridization between the S 3p and Fe 3d bands. Thus, the ordered moment is lowered. The increased covalency effect is also suggested by the lower hyperfine fields in greigite than magnetite,[38] with values in the range 30.5−31.4 kOe in greigite and 45.8−49.2 kOe in magnetite.[28]

Another contribution to the reduction of the saturation magnetization could be caused by surface spins. Previous research identified the existence of a core of aligned spins surrounded by a shell with moments inclined to the direction of the net magnetization in both $CoFe_2O_4$ and $NiFe_2O_4$ inverse

spinel nanocrystals with single magnetic domains. We note that a small proportion of particles in our sample are <10 nm in size (as indicated by the black arrow in Figure 3b and Figure S5 in the Supporting Information). A decreased magnetic moment was also observed in $NiFe_2O_4$ coated with an organic surfactant (oleic acid) due to surface spin canting.[39−41] If we magnify our magnetization loops at 5 K, it is clearly visible that the loop is open (inset to Figure 5A) for both positive and negative field sweeps up to 6 T. This opening indicates that some of the magnetic spins have a "switching field" larger than 6 T. A similar phenomenon was also observed in milled $NiFe_2O_4$ spinel.[42] We recorded first-order reversal curve (FORC) diagrams,[43] which are able to probe domain states and the extent of magnetostatic interactions (Figure 5C). The as-prepared samples have FORC distributions with concentric inner contours with high coercivity and strong magnetostatic interactions. This is characteristic for pseudo single-domain (PSD) greigite.[44] It is well-known that the spins are completely aligned by exchange interactions in sufficiently small PSD crystals, and that the rotation barriers induced by magneto-crystalline and magnetoelastic anisotropy can trap particles in two or more metastable orientations.[42] We should thus carefully consider the role of CTAB in the synthesis. It has been shown in previous work that CTAB can bond to metal cations via the polar end of the molecule. In our case, the $(C_{19}H_{42})N^+$ group in CTAB will interact with the Fe^{2+} or Fe^{3+} on the (111) faces of the growing crystals (Figure 3). The surface energy of these faces is thus decreased and finally preserved after the hydrothermal reaction.[45] This results in octahedral crystals with eight {111} faces as shown in the SEM images. The influence of the surfactant is still present in the final product, because complete removal of the surfactant from the crystals is difficult.[46] The CTAB groups will interact with the Fe^{2+} or Fe^{3+} at the surface, and thus result in a surface spin canting and a lower M_s.[46] The reduction in M_s is 4.2% in our sample, much smaller than the reduction of nearly 20% in nanocrystalline $NiFe_2O_4$ but comparable with that in surfactant-coated Fe_3O_4.[41]

3.4. Raman Spectra of Greigite. The lattice dynamics of greigite has not been well-studied; there is currently only one report on Raman spectroscopy of greigite at RT.[47] This sample was contaminated by mackinawite (FeS) and precise information on the positions of the greigite Raman peaks is still lacking. A group theory analysis on inverse-spinel greigite (space group $Fd\bar{3}m$ with a reduced unit cell (Fe_6S_8) that contains 14 atoms) predicts five Raman active modes: A_{1g}, E_g, and three T_{2g}.[48]

The measured Raman spectrum of greigite under vacuum is shown in Figure 6A, and the calculated and experimental frequencies of the Raman active modes are shown in Table 1. The A_{1g} mode represents the stretching of S atoms toward the tetrahedral site Fe atom. The calculated frequency is underestimated by 10% compared to the experimental value. The E_g mode represents the bending of $S-Fe_{tetra}-S$ bonds. The calculated frequency agrees well with the experimental value. Three T_{2g} modes that originate from the asymmetric bending of Fe−O were also observed. For the T_{2g1} and T_{2g2} modes, the calculated frequencies are underestimated by 11% and 5.5%. For the T_{2g3} mode, the calculated frequency agrees well with the experiment. Interestingly, when the measurement was carried out in air, only three Raman modes—with frequencies of 223 cm^{-1}, 290 cm^{-1}, and 405 cm^{-1}—were found. These can be assigned to the T_{2g3}, E_g, and T_{2g2} modes of Fe_3O_4,
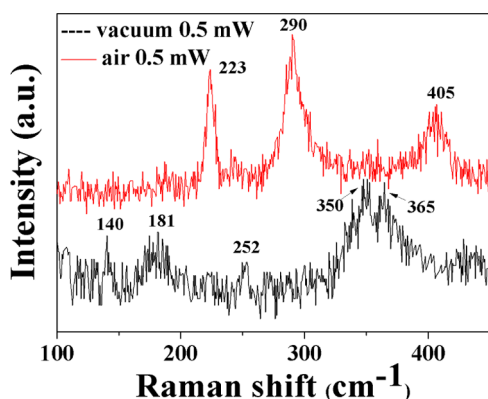
Figure 6. (A) Room-temperature (RT) Raman spectra of Fe_3S_4 measured in vacuum (black) and air (red).

Table 1. Measured and Calculated Zone Center Phonon Frequencies

	A_{1g}	E_g	$T_{2g\,1}$	$T_{2g\,2}$	$T_{2g\,3}$
phonon frequency (cm^{-1})					
expt	365	181	350	252	140
calc	327	180	312	238	142
ions involved	S	S	S, Fe_{tera}	S, Fe_{tetra}	S, Fe_{tetra}

respectively.[49] Because greigite is more covalent than magnetite, the frequencies of all the greigite modes are reduced by ~60%, with respect to magnetite. The Raman lines of greigite nearly disappeared in air, which indicates that the incident laser induced oxidation of the sample.

3.5. Electrical Transport Properties. The high purity of our sample offers the unique opportunity to investigate the electrical transport properties in Fe_3S_4. Four-probe resistance measurements were performed on pressed bar-shaped polycrystalline samples, as illustrated in the inset to Figure 7B. As shown in Figure 7A, the linear current–voltage (I–V) curves indicate that Ohm's law is obeyed from 20 K to RT, implying good contact between the sample and the electrodes. The temperature dependence of the resistivity was measured from 5 K to RT and is shown in Figure 7B. The resistivity increases from 10.5 mΩ cm at 5 K to 11.2 mΩ cm at 100 K, which is characteristic behavior for a metal. The resistivity then decreases upon further heating and reaches ~10.8 mΩ cm at RT, suggesting that there is a crossover from metallic to semiconductor-like behavior at ~100 K. This may originate

from the localization of carriers or a change in hopping mechanism with varying temperature.[50] Nevertheless, the resistivity is in the poor-metal range and is 40 times smaller than the values reported by Coey et al.[31] and Paolella et al.,[50] and is 7000 times smaller than the value measured on a single greigite microrod.[21] The lower resistivity can be attributed to the high purity and high crystallinity of the microcrystals. It should be noted that there is no sharp change in resistivity over the temperature range measured. The magnetization also changes continuously with temperature, as shown in Figure S6 in the Supporting Information. Therefore, we can conclude that greigite exhibits no analogue of the magnetite Verwey transition at ~120 K.

It has been demonstrated that Fe_3O_4 is a half metal, where the electronic density of states is 100% spin-polarized at the Fermi level. This has been confirmed by both band structure calculations and experiments.[51−53] However, our recent electronic structure calculations using the previously reported RT crystal structure of greigite show that it is a good metal.[8] We performed analogous calculations using the 20 K structure of greigite. As seen in Figure S7 in the Supporting Information, three bands intersect the Fermi energy for both the majority and minority-spin directions. The band dispersion is somewhat larger for the majority-spin direction. This band structure indicates that greigite is also a good metal at 20 K. Interestingly, we note that a study of epitaxial Fe_3O_4 (100) films grown on a W (100) single crystal indicated that the spin polarization at the Fermi level decreased dramatically, in comparison with bulk samples.[54] This implies that the Fe_3O_4 (100) surface shows metallic behavior rather than the half metallic behavior exhibited by bulk samples. Considering the micrometer size and surfactant-coated surfaces of our greigite crystals, it is reasonable to conclude from the current evidence that our samples are representative of bulk greigite and that it exhibits metallic behavior, especially at lower temperatures.

3.6. Electrochemical Properties. Using our greigite-containing coin cells, we performed up to 100 charge–discharge cycles between 0.005 V and 3 V at a current density of 100 mA/g and at RT. The open-circuit voltage (OCV) of the cells is ~3.0 V and curves for selected cycles are shown in Figure 8A. In the first cycle, the voltage decreases sharply to 1.7 V and reaches a plateau at a capacity of ~150 mAh/g. A second voltage plateau is observed at ~1.4 V up to a capacity of ~600 mAh/g, followed by a steady decrease to the cutoff voltage of 0.01 V. This indicates that the discharge process involves a two-
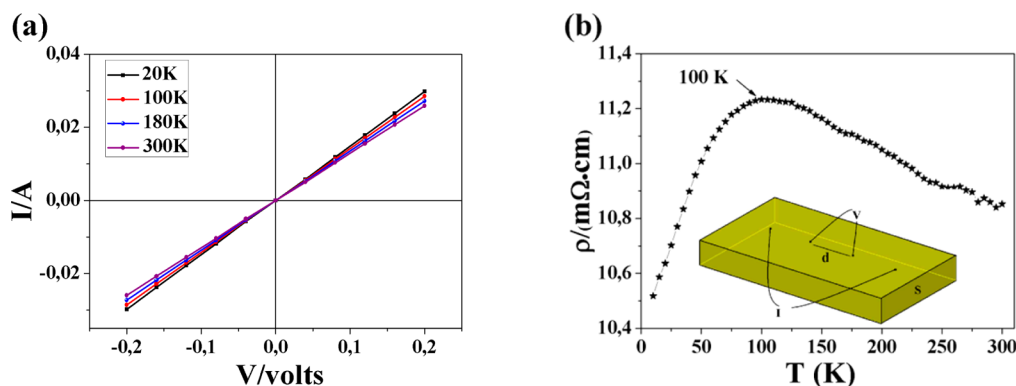
Figure 7. (A) Four-probe current–voltage (I–V) measurements at 20, 100, 180, and 300 K. (B) Resistivity of greigite between 5 K and 300 K, and the corresponding contact geometry (inset).
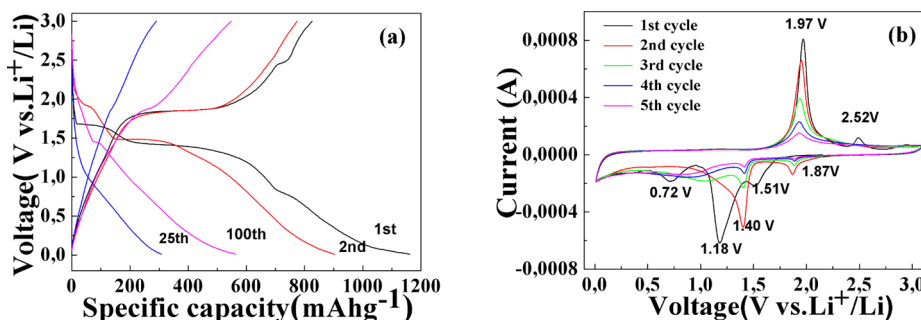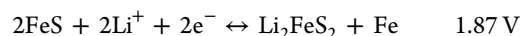
Figure 8. (A) Galvanostatic charge−discharge curves of Fe_3S_4 in the voltage range 0.005−3.0 V (versus Li) at a current of 100 mA g^{-1}. (B) Cyclic voltammogram of the as-prepared Fe_3S_4 electrode at a scan rate of 0.1 mV s^{-1} in the range of 0.01−3.0 V (vs Li$^+$/Li).

phase reaction.[55] For our greigite cell, the first intercalation cycle gives a discharge capacity of 1161 mAh/g and a corresponding charge capacity of 1139 mAh/g. This capacity is 10 times larger than that previously reported for battery anodes comprised of greigite nanoparticles.[50] The first charge profile has a long plateau at ∼1.87 V, followed by a shorter one at ∼2.5 V, which, again, is consistent with a two-phase reaction. It is interesting to note that the initial discharge capacity is much higher than the theoretical value of 785 mAh/g.[56] This phenomenon has also been reported for Fe_3O_4 and Fe_2O_3 and was ascribed to the reversible formation and decomposition of a polymeric gel-like film on the particle electrode surface. This film is formed by kinetically governed electrolyte degradation driven by active metal (Fe) nanoparticles.[57,58] In the second cycle, the discharge capacity decreases to 903 mAh/g, while the charge capacity is 960 mAh/g. These values further decrease to 674 mAh/g and 554 mAh/g in the fifth cycle. The reduction in capacity results from large volume changes of the greigite microcrystals after lithium insertion, resulting in disintegration of the crystals and loss of the connection between the electrode materials and the current collector.[59] The capacity stops decreasing after ∼20 cycles and then increases gradually to 563 mAh/g in the 100th cycle (also see Figure S8 in the Supporting Information). This is still much larger than the capacity of cells with graphite as the electrode material (320−340 mAh/g).[58] The reason for the stability of our greigite cell is not clear. We suggest that the nanostructured Fe^0−amorphous Li_2S composite formed during the first discharge reaction needs several cycles to form a stable solid electrolyte interphase (SEI) film, allowing the greigite crystals to percolate throughout and establish intimate contact with the current collector.
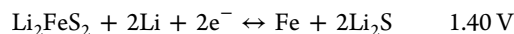
In order to understand the electrochemical process, we performed cyclic voltammetry (CV) at a scanning rate of 0.1 mV s^{-1} as shown in Figure 8B. In the first cycle, the reduction peak at ∼1.18 V with a shoulder at ∼1.51 V indicates the insertion of Li followed by the reduction of both Fe^{3+} and Fe^{2+} ions to Fe^0, forming the Fe^0-Li_2S composite as described above.[60] The reduction peak at 0.72 V is consistent with the formation of a SEI film. This is also the main reason for the irreversible capacity during the discharge process. In the subsequent oxidation scan, the material is converted to Li_2FeS_2 at ∼1.97 V and then to FeS at ∼2.52 V by the reaction of Li_2FeS_2 with the resulting Fe. These peaks nearly coincide with the two voltage plateaus in the galvanostatic charging curve in Figure 8A. The first and second CV profiles are different, indicating a change in mechanism in the battery. The sharp anodic peak at ∼1.97 V remains, but the peak at 2.52 V disappears. In addition, the cathodic peaks are shifted to more-

positive potentials from the second cycle onward, because of structural modification after the first cycle. The reduced polarization in this process indicates better reversibility. The detailed reaction in the second discharge cycle can be described as follows:

(1):

$$2FeS + 2Li^+ + 2e^- \leftrightarrow Li_2FeS_2 + Fe \qquad 1.87\,V$$

(2):

$$Li_2FeS_2 + 2Li + 2e^- \leftrightarrow Fe + 2Li_2S \qquad 1.40\,V$$

The cycling performance of the Fe_3S_4 electrode at a current density of 100 mA/g is displayed in Figure S8 in the Supporting Information. The discharge capacity decreases continuously from 1161 mAh/g at the first cycle to 310 mAh/g at the 25th cycle. The rate of decrease in capacity is maximum between the first and second cycles and becomes much flatter during cycles 10−25. The initial loss of capacity may result from an incomplete conversion reaction and the irreversible loss of Li ions due to the formation of a SEI layer, as discussed above. The subsequent capacity losses are perhaps caused by defects in the greigite crystals, the structure of which is shown in Figure 3C. Small numbers of Li ions might be trapped in these defects, thus inducing the irreversible capacity.[61] Interestingly, the discharge capacity increases from the 25th cycle onward and reaches 563 mAh/g after 100 cycles. This increase of capacity might be sustained over more cycles if the charge/discharge process is repeated. Similar results have been reported in many other studies, especially those with sulfides as the electrode material.[61−63] Reasons for this phenomenon are still unclear, but it might be linked to an activation process in the electrode. As the number of cycles increases, the increase in capacity is always accompanied by a decrease in the electrode impedance. The capacitance of the electrode/electrolyte interfaces was also observed to increase with cycling for some sulfides.[63] Defects and vacancies in the crystals, which trap Li ions, will tend to become more extended and facilitate the insertion of more Li ions with further cycling. In addition, the high crystallinity and low resistivity of our sample can also promote the uniform and stable delivery of electrons, further facilitating the deintercalation/intercalation of Li ions. Consequently, the transfer of electrons and Li$^+$ is more effective at the interface of the active materials and the electrolyte.[64]

The octahedral shape of our crystals, comprising eight (111) surfaces, might be a key factor in the high electrochemical performance. Figure 1 illustrates the atomic configurations of the (001) and (111) surfaces. The (111) plane contains a much greater density of Fe^{3+}/Fe^{2+} cations than the (001) plane.

Research on the charge/discharge mechanism of spinel structures has shown that the redox reaction of M^{n+}/M^0 (where M is a transition metal) is related to the discharge capacity.[65,66] The morphology of our greigite crystals, which is controlled by the surfactant, will thus facilitate fast $Fe^{3+}(Fe^{2+})/Fe^0$ redox reactions, resulting in excellent cycling performance as well as a high capacity.

4. CONCLUSIONS

We have synthesized highly pure, monodisperse greigite microcrystals using a surfactant-based hydrothermal method. We measure a saturation magnetization of 3.74 μ_B, close to the expected value of 4 μ_B (assuming a purely ionic model) and a resistivity that is 40 times lower than all previous reports on greigite, indicating a metallic-like ground state and the high quality of our samples. The saturation magnetization is slightly lower than 4 μ_B due to the appreciable degree of covalency involved in Fe−S bonding, as well as the possible canting of surface spins caused by the presence of surfactant molecules bonded to the surface. Greigite is different to magnetite in that it does not exhibit a Verwey transition down to 5 K, the lowest temperature investigated here. However, in contrast to previous reports, greigite is similar to magnetite in that both materials have a [111] magnetic easy axis. As an anode material for Li-ion batteries, greigite exhibits a high initial capacity of 1161 mAh/g and 562.9 mAh/g after 100 cycles. This excellent performance, combined with the fact that greigite is abundant and environmentally friendly, makes it a candidate to replace generally used graphite.

■ ASSOCIATED CONTENT

ⓢ Supporting Information

Details of electronic band structure and phonon calculations, XRD pattern of the as-prepared sample at 20 K, EDS spectrum of the sample, Mössbauer spectrum at 80 K and details of fits to the Mössbauer spectra, magnetization versus field loops measured at 300 K, TEM images of small particles, magnetization as a function of temperature, calculated band structures for majority and minority spins, discharge capacity of the Fe_3S_4 electrode up to 100 cycles. This material is available free of charge via the Internet at http://pubs.acs.org.

■ AUTHOR INFORMATION

Corresponding Author

*E-mail: t.t.m.palstra@rug.nl.

Notes

The authors declare no competing financial interest.

■ ACKNOWLEDGMENTS

■ REFERENCES

(1) Skinner, B. J.; Erd, R. C.; Grimaldi, F. S. *Am. Mineral.* **1964**, *49* (5−6), 543−555.

(2) Roberts, A. P.; Weaver, R. *Earth Planet Sci. Lett.* **2005**, *231* (3−4), 263−277.

(3) Vasiliev, I.; Franke, C.; Meeldijk, J. D.; Dekkers, M. J.; Langereis, C. G.; Krijgsman, W. *Nat. Geosci.* **2008**, *1* (11), 782−786.

(4) Snowball, I.; Thompson, R. *J. Quat. Sci.* **1988**, *3* (2), 121−125.

(5) Rickard, D.; Luther, G. W. I. *Chem. Rev.* **2007**, *107* (2), 514−562.

(6) Lapen, T. J.; Righter, M.; Brandon, A. D. *Science* **2010**, *328* (April), 347−351.

(7) McKay, D. S.; Everett, K. G., Jr.; Thomas-keprta, K. L.; Vali, H.; Romanek, C. S.; Clemett, S. J.; Chillier, X. D. F.; Maechling, C. R.; Zare, R. N. *Science* **1996**, *273* (5277), 924−930.

(8) Zhang, B. M.; de Wijs, G. A.; de Groot, R. A. *Phys. Rev. B* **2012**, *86*, 020406.

(9) Jia, X. L.; Chen, Z.; Cui, X.; Peng, Y. T.; Wang, X. L.; Wang, G.; Wei, F.; Lu, Y. F. *ACS Nano* **2012**, *6* (11), 9911−9919.

(10) Cao, F.; Hu, W.; Zhou, L.; Shi, W.; Song, S.; Lei, Y. *Dalton. Trans.* **2009**, *14* (42), 9246−9252.

(11) Chang, Y. S.; Savitha, S.; Sadhasivam, S.; Hsu, C. K.; Lin, F. H. *J. Colloid Interface Sci.* **2011**, *363* (1), 314−319.

(12) Feng, M.; Lu, Y.; Yang, Y.; Zhang, M.; Xu, Y. J.; Gao, H. L.; Dong, L.; Xu, W. P.; Yu, S. H. *Sci. Rep.* **2013**, *3*, 2994.

(13) Chang, L.; Rainford, B. D.; Stewart, J. R.; Ritter, C.; Roberts, A. P.; Tang, Y.; Chen, Q. *J. Geophys. Res.* **2009**, *114*, B07101.

(14) Roberts, A. P.; Chang, L.; Rowan, C. J.; Horng, C. S.; Florindo, F. *Rev. Geophys.* **2011**, *49* (1), RG1002.

(15) Letard, I.; Sainctavit, P.; Menguy, N.; Valet, J. P.; Isambert, A.; Dekkers, M.; Gloter, A. *Phys. Scr.* **2005**, *T115*, 489−491.

(16) Dekkers, M. J.; Passier, H. F.; Schoonen, M. A. A. *Geophys. J. Int.* **2000**, *141* (3), 809−819.

(17) Akhtar, M.; Akhter, J.; Malik, M. A.; O'Brien, P.; Tuna, F.; Raftery, J.; Helliwell, M. *J. Mater. Chem.* **2011**, *21* (26), 9737−9745.

(18) Zhang, Y.; Du, Y.; Xu, H.; Wang, Q. *CrystEngComm* **2010**, *12* (11), 3658−3663.

(19) Xing, R.; Liu, S. *Nanoscale* **2012**, *4* (10), 3135−3140.

(20) Lebedev, O. I.; Turner, S.; Liu, S.; Cool, P.; Van Tendeloo, G. *Nanoscale* **2012**, *4* (5), 1722−1727.

(21) He, Z.; Yu, S. H.; Zhou, X.; Li, X.; Qu, J. *Adv. Funct. Mater.* **2006**, *16* (8), 1105−1111.

(22) Chang, L.; Roberts, A. P.; Muxworthy, A. R. *Geophys. Res. Lett.* **2007**, *34*, 1−6.

(23) Wang, J.; Cao, S.-H.; Wu, W.; Zhao, G.-m. *Phys. Scr.* **2011**, *83* (4), 045702.

(24) Devey, A.; Grau-Crespo, R.; de Leeuw, N. *Phys. Rev. B* **2009**, *79* (19), 195126.

(25) Bauer, E.; Man, K. L.; Pavlovska, A.; Locatelli, A.; Menteş, T. O.; Niño, M. A.; Altman, M. S. *J. Mater. Chem. A* **2014**, *2* (6), 1903.

(26) Lennie, A. R.; Redfern, S. A. T. *Am. Mineral.* **1997**, *82*, 302−309.

(27) Chang, L.; Roberts, A. P.; Tang, Y.; Rainford, B. D.; Muxworthy, A. R.; Chen, Q. *J. Geophys. Res.* **2008**, *113*, B06104.

(28) Lyubutin, I. S.; Lin, C. R.; Korzhetskiy, Y. V.; Dmitrieva, T. V.; Chiang, R. K. *J. Appl. Phys.* **2009**, *106* (3), 034311.

(29) Lyubutin, I. S.; Starchikov, S. S.; Lin, C. R.; Lu, S. Z.; Shaikh, M. O.; Funtov, K. O.; Dmitrieva, T. V.; Ovchinnikov, S. G.; Edelman, I. S.; Ivantsov, R. *J. Nanopart. Res.* **2013**, *15* (1), 1397−1409.

(30) Erd, R. C.; Evans, H. T., Jr. *J. Am. Chem. Soc.* **1956**, *78* (9), 2017.

(31) Furukawa, F.; Barnes, H. L. *Geochim. Cosmochim. Acta* **1996**, *60* (19), 3581−3591.

(32) Van Diepen, A. M. *Phys. Lett.* **1976**, *57A* (4), 354−356.

(33) Coey, J. M. D.; Spender, M. R.; Morrish, A. H. *Solid State Commun.* **1970**, *8*, 1605−1608.

(34) De Grave, E.; Persoons, R.; Vandenberghe, R.; de Bakker, P. *Phys. Rev. B* **1993**, *47* (10), 5881−5893.

(35) Chang, L.; Winklhofer, M.; Roberts, A. P.; Dekkers, M. J.; Horng, C.-S.; Hu, L.; Chen, Q. *Geochem., Geophys., Geosyst.* **2012**, *13*, 1−19.

(36) Winklhofer, M.; Chang, L.; Eder, S. H. K. *Geochem., Geophys., Geosyst.* **2014**, *15* (4), 1558−1579.

(37) Chikazumi, S. *Physics of Magnetism*; Wiley: New York, 1964; p 277.

(38) Chang, L.; Rainford, B. D.; Stewart, J. R.; Ritter, C.; Roberts, A. P.; Tang, Y.; Chen, Q. *J. Geophys. Res.* **2009**, *114*, B07101.

(39) Morr, A. H.; Haneda, K.; Morrish, A. H. *J. Appl. Phys.* **1981**, *52* (3), 2496−2498.

(40) Lin, D.; Nunes, A. C.; Majkrzak, C. F.; Berkowitz, A. E. *J. Magn. Magn. Mater.* **1995**, *145*, 343−348.

(41) Berkowitz, A.; Lahut, J.; Jacobs, I.; Levinson, L.; Forester, D. *Phys. Rev. Lett.* **1975**, *34* (10), 594−597.

(42) Kodama, R. H.; Berkowitz, A. E.; McNiff, E. J.; Foner, S. *Phys. Rev. Lett.* **1996**, *77*, 394−397.

(43) Pike, C. R.; Roberts, A. P.; Verosub, K. L. *J. Appl. Phys.* **1999**, *85* (9), 6660−6667.

(44) Roberts, A. P.; Liu, Q.; Rowan, C. J.; Chang, L.; Carvallo, C.; Torrent, J.; Horng, C.-S. *J. Geophys. Res.* **2006**, *111*, B12S35.

(45) Wang, N.; Cao, X.; Guo, L.; Yang, S. H.; Wu, Z. Y. *ACS Nano* **2008**, *2* (2), 184−190.

(46) Niu, Z.; Li, Y. *Chem. Mater.* **2014**, *26*, 72−83.

(47) Rémazeilles, C.; Saheb, M.; Neff, D.; Guilminot, E.; Tran, K.; Bourdoiseau, J.-A.; Sabot, R.; Jeannin, M.; Matthiesen, H.; Dillmann, P.; Refait, P. *J. Raman Spectrosc.* **2010**, *41* (11), 1425−1433.

(48) White, W. B.; Deangelis, B. A. *Spectrochim. Acta A* **1967**, *23A*, 985−995.

(49) Shebanova, O. N.; Lazor, P. *J. Solid State Chem.* **2003**, *174* (2), 424−430.

(50) Paolella, A.; George, C.; Povia, M.; Zhang, Y.; Krahne, R.; Gich, M.; Genovese, A.; Falqui, A.; Longobardi, M.; Guardia, P.; Pellegrino, T.; Manna, L. *Chem. Mater.* **2011**, *23*, 3762−3768.

(51) Chang, M. T.; Chou, L. J.; Hsieh, C. H.; Chueh, Y. L.; Wang, Z. L.; Murakami, Y.; Shindo, D. *Adv. Mater.* **2007**, *19* (17), 2290−2294.

(52) Groot, R. A.; Mueller, F. M. *Phys. Rev. Lett.* **1983**, *50* (25), 2024−2027.

(53) Zhang, D.; Liu, Z.; Han, S.; Li, C.; Lei, B. *Nano Lett.* **2004**, *4* (11), 2151−2155.

(54) Fonin, M.; Pentcheva, R.; Dedkov, Y. S.; Sperlich, M.; Vyalikh, D. V.; Scheffler, M.; Rüdiger, U.; Güntherodt, G. *Phys. Rev. B* **2005**, *72* (10), 104436.

(55) Sharma, N.; Guo, X.; Du, G.; Guo, Z.; Wang, J.; Wang, Z.; Peterson, V. K. *J. Am. Chem. Soc.* **2012**, *134* (18), 7867−7873.

(56) Chen, J.; Xu, L.; Li, W.; Gou, X. *Adv. Mater.* **2005**, *17* (5), 582−586.

(57) Xu, J. S.; Zhu, Y. J. *ACS Appl. Mater. Interfaces* **2012**, *4* (9), 4752−4757.

(58) Yu, Y.; Chen, C. H.; Shui, J. L.; Xie, S. *Angew. Chem., Int. Ed.* **2005**, *44* (43), 7085−7089.

(59) Wang, X. L.; Han, W. Q.; Chen, H.; Bai, J.; Tyson, T. A; Yu, X. Q.; Wang, X. J.; Yang, X. Q. *J. Am. Chem. Soc.* **2011**, *133* (51), 20692−20695.

(60) Reddy, M. V.; Yu, T.; Sow, C. H.; Shen, Z. X.; Lim, C. T.; Subba Rao, G. V.; Chowdari, B. V. R. *Adv. Funct. Mater.* **2007**, *17* (15), 2792−2799.

(61) Chang, K.; Wang, Z.; Huang, G. H.; Li, H.; Chen, W. X.; Lee, J. Y. *J. Power Sources* **2012**, *201*, 259−266.

(62) Du, Y.; Yin, Z.; Zhu, J.; Huang, X.; Wu, X. J.; Zeng, Z.; Yan, Q.; Zhang, H. *Nat. Commun.* **2012**, *3*, 1−7.

(63) Chang, K.; Geng, D. S.; Li, X. F.; Yang, J. L.; Tang, Y. J.; Cai, M.; Li, R. Y.; Sun, X. L. *Adv. Energy Mater.* **2013**, *3* (7), 839−844.

(64) Xiong, Q. Q.; Tu, J. P.; Lu, Y.; Chen, J. *J. Phys. Chem. C* **2012**, *116*, 6495−6502.

(65) Xiao, X.; Liu, X.; Zhao, H.; Chen, D.; Liu, F.; Xiang, J.; Hu, Z.; Li, Y. *Adv. Mater.* **2012**, *24* (42), 5762−5766.

(66) Binotto, G.; Larcher, D.; Prakash, A. S.; Urbina, R. H.; Hegde, M. S.; Tarascon, J. M. *Chem. Mater.* **2007**, *19* (12), 3032−3040.

5829

dx.doi.org/10.1021/cm501493m | *Chem. Mater.* 2014, 26, 5821−5829